

pubs.acs.org/ac Article

# A Visual Hydrogen Sensor Prototype for Monitoring Magnesium Implant Biodegradation

Michael E. Smith, Daniel P. Rose, Xiaoyu Cui, Angela L. Stastny, Peng Zhang,\* and William R. Heineman\*



Cite This: Anal. Chem. 2021, 93, 10487–10494



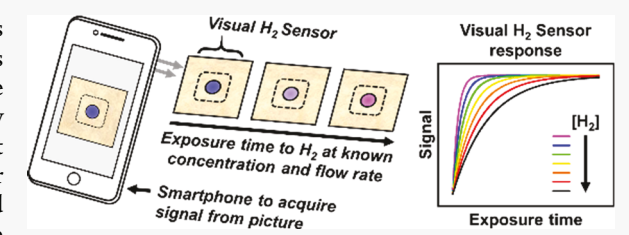
**ACCESS** 

Metrics & More

Article Recommendations

Supporting Information

**ABSTRACT:** Alternative metals such as magnesium (Mg) and its alloys have been recently developed for clinical applications such as temporary implants for bone and tissue repair due to their desirable mechanical properties and ability to biodegrade harmlessly *in vivo* by releasing Mg<sup>2+</sup>, OH<sup>-</sup>, and H<sub>2</sub> as biodegradation products. The current methods for monitoring *in vivo* Mg-alloy biodegradation are either invasive and/or costly, complex, or require large equipment and specially trained personnel, thus making real-time and point-of-care monitoring of Mg-alloy implants problematic. Therefore, innovative



methods are critically needed. The objective of this research was to develop a novel, thin, and wearable visual  $H_2$  sensor prototype for noninvasive monitoring of *in vivo* Mg-implant biodegradation in medical research and clinical settings with a fast response time. In this work, we successfully demonstrate such a prototype composed of resazurin and catalytic bimetallic gold-palladium nanoparticles (Au-Pd NPs) incorporated into a thin agarose/alginate hydrogel matrix that rapidly changes color from blue to pink upon exposure to various levels of  $H_2$  at a constant flow rate. The irreversible redox reactions occurring in the sensor involve  $H_2$ , in the presence of Au-Pd NPs, converting resazurin to resorufin. To quantify the sensor color changes, ImageJ software was used to analyze photographs of the sensor taken with a smartphone during  $H_2$  exposure. The sensor concentration range was from pure  $H_2$  down to limits of detection of 6 and 8  $\mu$ M  $H_2$  (defined via two methods). This range is adequate for the intended application of noninvasively monitoring *in vivo* Mg-alloy implant biodegradation in animals for medical research and patients in clinical settings.

etals such as stainless steel, Ti, and Co–Cr have been commonly used as permanent fixtures for orthopedic, craniomaxillofacial, and cardiovascular applications such as the repair of broken bones and tissues. 1-8 Though these types of implants have historically been very effective, several problems are associated with their use such as bone loss via stress shielding<sup>9,10</sup> as well as the release of toxic metal ions and particles after long-term in vivo implant corrosion that leads to inflammatory responses with subsequent tissue and bone losses. 11-14 Another significant disadvantage is that implants of this type often require second surgeries after initial implantation, which gives rise to additional surgery risks, patient stress, and high cost of care. Almost 30% of implants of the aforementioned variety are removed later because of complications or the need to accommodate a still-growing child.<sup>14</sup> For these reasons, researchers have pursued alternatives such as magnesium (Mg) and its alloys in the form of plates, screws, and pins for fracture fixation and other clinical applications due to their unique properties.<sup>3,15</sup>

The most important features of Mg for fracture fixation applications are the fact that it exhibits adequate mechanical strength that reduces stress shielding<sup>24</sup> and it biodegrades or corrodes in biological fluids to generate  $Mg^{2+}$  ions,  $OH^-$  ions, and  $H_2$  gas according to eq 1, thus eliminating the need for a second surgery for removing an implant once the tissue has

completely healed.<sup>2,3,5,6,8,15,24</sup> A key parameter for the efficacy of Mg-based materials for fracture fixation and other *in vivo* applications is to control the rate of biodegradation such that the implant can dissolve away harmlessly within the body while the mechanical stiffness/strength of the temporary implant slowly decreases and the damaged tissue increases in stiffness/strength over time.<sup>24</sup> Overall, the biocompatibility and desirable mechanical properties of Mg-based materials make them attractive candidates for use as temporary biodegradable implants.<sup>3,19,24–26</sup>

$$Mg + 2H_2O \rightarrow Mg^{2+} + 2OH^- + H_2$$
 (1)

However, monitoring *in vivo* Mg-implant biodegradation represents a substantial challenge. Current techniques include radiography, ultrasonography, micro-computed tomography, synchrotron radiation micro-computed tomography, magnetic resonance imaging (MRI), blood evaluation in combination

Received: March 23, 2021 Accepted: July 6, 2021 Published: July 19, 2021





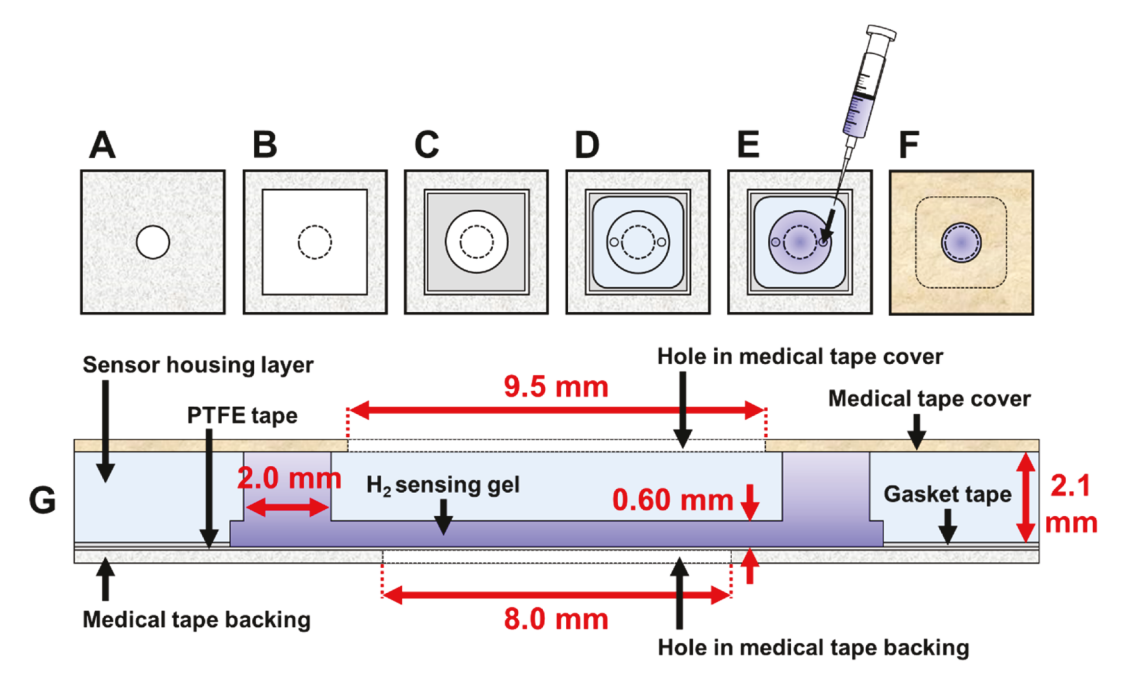


Figure 1. Visual  $H_2$  sensor fabrication. (A) An 8 mm hole is punched into an  $\sim 3.5$  in.<sup>2</sup> square piece of double-lined medical tape. One of the liners is peeled off to expose a sticky surface facing upward. The medical tape is then affixed to a 3 in.  $\times$  4 in. glass slide using a common transparent tape. (B) A piece of  $\sim 1$  in.<sup>2</sup> PTFE tape is placed above the hole in the medical tape. (C) A 15 mm hole is punched into a piece of double-lined gasket tape. The liner for the acrylic adhesive side is peeled off, and the gasket tape is affixed to the PTFE and medical tapes. The liner for the silicone adhesive is then peeled off. (D) The sensor housing layer is placed onto the silicone adhesive of the gasket tape. (E) The  $H_2$  sensing gel is injected into the sensor housing layer. (F) A 9.5 mm hole is punched into a piece of tan medical tape, and this final layer is affixed to the top of the sensor to seal all layers. (G) Cross-sectional schematic with dimensions of the final sensor with the final liner of the medical tape removed.

with techniques such as inductively coupled mass spectrometry, and histological analyses. 16,27 These techniques are accompanied by several shortcomings. First, they only provide segmented or non-real-time representations of in vivo implant biodegradation and fail to reveal the fundamentals of timedependent in vivo biodegradation processes.<sup>27</sup> The histological and blood evaluation procedures are invasive and involve the collection of biofluids to examine the distribution of biodegradation products, such as ions, surrounding the implantation site.<sup>27</sup> Additionally, long-term patient exposure to radiation such as X-rays and excessive heat generation from high-frequency sound waves can dangerously affect living tissues. 27-29 MRI results can become difficult to interpret since metal implants have been shown to heat surrounding tissues.<sup>2</sup> From an economic standpoint, many of these current monitoring modalities require large and expensive instrumentation that require specific handling, specially trained personnel, and specialized environments to make measurements.<sup>27</sup> Furthermore, the post-analysis time to work up and interpret raw data impedes real-time monitoring.<sup>27</sup> Collectively, the shortcomings of these current methods make real-time and point-of-care monitoring of in vivo Mg-implant biodegradation unfeasible. Thus, there is a critical need for innovative methods to monitor the biodegradation of Mg-alloys.

The ideal method should be noninvasive and use low-cost materials and/or instrumentation with integrated data processing features that are easily handled and operated. With respect to the development of such methods, we have previously shown in several animal studies that a fraction of  $\rm H_2$  liberated as a product from Mg-implant biodegradation can be detected noninvasively in near-real-time through the skin at levels ranging from ~10 to ~700  $\mu \rm M$  by placing electrochemical or visual  $\rm H_2$  sensors on animal skin directly above the

implants as they biodegraded in vivo. 1,2,6,8,15,30,31 Since the measured H2 levels in these animal studies strongly correlated with the biodegradation rates measured by a highly accurate mass loss method of explanted implants, these noninvasive H<sub>2</sub>sensing methods are considered to be fast, reliable, and accurate representations of the extent of Mg-implant biodegradation *in vivo*. <sup>8,31</sup> Despite these breakthroughs, an electrochemical H2 sensor of ~50 µm in surface diameter afforded excellent sensitivity, yet the sensor and instrumentation are costly, complex, require regular calibration, need technical skill levels for proper use, and require numerous measurements if mapping of H<sub>2</sub> levels is desired. A visual H<sub>2</sub> sensor of  $\sim 10 \,\mu \text{m}$  in thickness and  $\sim 1 \,\text{cm}^2$  in surface area gave rise to a detailed mapping of H<sub>2</sub> levels above the implants that could be easily monitored using a smartphone, but the exposure time required to induce detectable color changes took several hours at low concentrations, which makes the sensing platform nonpractical for the intended application.<sup>2,6</sup> To overcome these limitations, the objective of this research was to develop a novel, thin, and wearable visual H<sub>2</sub> sensor prototype for noninvasive monitoring of in vivo Mg-implant biodegradation in medical research and clinical settings with a fast response time. The envisioned use for the sensor would be a direct application to the patient skin directly above the Mg implant such that the extent of the color change resulting from the reaction with H<sub>2</sub> can be captured via a photograph, and the information can be used by doctors to consult patients.

Previously, we tested the reactivity of various indicator molecules combined with catalytic bimetallic gold-palladium nanoparticles (Au-Pd NPs) in solution for an irreversible, visual response to  $\rm H_2$ . The combination of resazurin and Au-Pd NPs was the indicator/catalyst system best suited for incorporation into a novel visual  $\rm H_2$  sensor because (1) this

system had the fastest visual color change response to H<sub>2</sub> at levels relevant to in vivo Mg-implant biodegradation compared to the other indicator/Au-Pd NP systems tested, (2) the observed redox chemistry with H2 followed well-understood reaction pathways, and (3) resazurin and its redox products are nontoxic and appropriate for medical applications.<sup>32</sup> The redox reactions and associated color changes of the resazurin/Au-Pd NP system upon reaction with  $H_2$  at pH  $\sim$ 7.5 are shown in eq 2 where resazurin (blue color) undergoes an irreversible reduction to form the highly luminescent resorufin (pink color) with a subsequent reduction to dihydroresorufin (colorless) that is reversible in the presence of O2. Despite the reversibility of the subsequent reaction involving resorufin and dihydroresorufin, the resazurin/Au-Pd NP system was hypothesized to serve well as the visual color change mechanism for sensor development since the initial irreversible reduction that forms resorufin would likely be the only color transition observed at low levels of H2 exposure associated with in vivo Mg-implant biodegradation.

$$\begin{array}{c} \circ \\ \circ \\ \\ \hline \\ Resazurin \end{array} \xrightarrow{2H^r+2e^-} \\ \circ \\ \hline \\ Resorufin \end{array} \xrightarrow{3H^r+2e^-} \\ \hline \\ O_2(g) \\ \hline \\ Dihydroresorufin \end{array} \xrightarrow{0} \\ O_3(g) \\ O_3(g) \\ O_4(g) \\ O_4$$

In this work, we demonstrate a novel, thin, and wearable visual H<sub>2</sub> sensor prototype composed of resazurin and Au-Pd NPs incorporated into a thin alginate/agarose (AA) hydrogel matrix that rapidly changed color from blue to pink upon exposure to various levels of H<sub>2</sub> at a constant flow rate. To quantify sensor color changes, ImageJ software was used to analyze photographs of sensors taken with a smartphone during H2 exposure. The color from these photographs was split into red, green, and blue channels by ImageJ software. The ratio of the time-dependent red color during H<sub>2</sub> exposure  $(r_t)$  and red color without H<sub>2</sub> exposure  $(r_0)$ , i.e.,  $r_t/r_0$ , was used to quantify sensor color changes. Since the H2 sensor exhibited rapid visual color changes upon reaction with H2 at levels comparable to that detected from in vivo biodegradation of subcutaneous Mg-alloy implants in animal studies, 1,2,6,8,15,30,31 the sensors developed in this work are potentially useful for noninvasively monitoring the in vivo biodegradation of Mg implants in medical research animal studies and patients in clinical settings.

#### ■ EXPERIMENTAL SECTION

Chemicals, Materials, and Instrumentation. A description of the chemicals, materials, and instrumentation used herein is provided in the Supporting Information (SI).

**Visual H<sub>2</sub> Sensor Construction.** Bandage-like visual H<sub>2</sub> sensors were constructed according to Figure 1. An 8 mm hole was punched in the middle of an ~3.5 in.<sup>2</sup> square piece of white-colored medical tape (3M, #9917) (Figure 1A). One of the liners was peeled off to expose a sticky surface facing upward. This tape was affixed to a glass slide using a common transparent tape. An ~1 in.<sup>2</sup> square piece of white polytetrafluoroethylene (PTFE) tape (McMaster-Carr, #6802 K14) was cut and placed onto the sticky surface of the medical tape to cover the hole (Figure 1B). A piece of double-sided and double-lined gasket tape (McMaster-Carr, #7213A27) was cut into an ~1 in.<sup>2</sup> square, and a 15 mm hole was then punched out in the middle. This gasket tape had a silicone adhesive on one side and an acrylic adhesive on the other. Both liners were removed, and the gasket tape was placed on top of

the PTFE layer with the silicone adhesive side facing upward (Figure 1C). An optically transparent sensor housing layer made of poly(dimethylsiloxane) (PDMS) was fabricated according to Figure S1 (SI) and placed on top of the silicone adhesive of the gasket tape to adjoin the PDMS to the PTFE layer attached to the white-colored medical tape (Figure 1D). Doing so created a thin void between the PTFE and sensor housing layers with an  $\sim 115 \mu L$  volume such that a H<sub>2</sub> sensing gel, composed of an AA hydrogel, resazurin, and Au-Pd NPs, could be injected into this void. The sensor housing layer was fabricated by machining aluminum plates to the shape and dimensions described in Figure S1A (SI). The plates were then placed in Petri dishes (Figure S1B, SI). A PDMS solution was prepared according to the manufacturer's instructions, and 4.7 g of it was added into a Petri dish (Figure S1C, SI) and cured for 3 days at room temperature in a fume hood. The cured PDMS was removed and cut into a square-like pattern using a cutting tool (Figure S1D, SI). This process yielded a 2.1 mm thick and 24 mm wide transparent piece of PDMS that had a 15 mm diameter by 0.5 mm deep circular depression in the middle to house the H2 sensing gel. Two holes of 2 mm diameter were then punched out along the edge of the circular depression (Figure S1E, SI) to serve as inlets and outlets for subsequent injection of the H2 sensing gel into a layered assembly.

To make the H<sub>2</sub> sensing gel, an AA hydrogel solution was prepared according to the method of Zeng et al.<sup>33</sup> with modifications. Two percent (m/V) solutions of alginate and agarose were prepared individually in 1× phosphate-buffered saline (PBS) (referred to as alginate and agarose solutions herein). A standard microwave was used to dissolve the agarose (~2 min), while an autoclave was used to dissolve the alginate (120 °C for 2 h). Five milliliters of alginate solution and 4.425 mL of agarose solution were combined in a 25 mL scintillation vial, vortexed briefly, and then placed on a hot plate at 60 °C. Five hundred and twenty-five microliters of 1 mM resazurin in 1× PBS buffer and 50  $\mu$ L of Au-Pd NP master solution prepared according to Smith et al.<sup>32</sup> were combined in a microcentrifuge tube, vortexed briefly, and then left to rest in the dark for at least 30 min before being added to the AA hydrogel solution. This solution was vortexed and then kept at 60 °C. This combination of resazurin and Au-Pd NPs in the AA hydrogel matrix will be referred to as the H2 sensing gel herein. The H<sub>2</sub> sensing gel was loaded into a syringe, then injected into the inlet of the H<sub>2</sub> sensor housing layer (Figure 1E), and left to gel at room temperature for 30 min, thereby creating a thin layer of H2 sensing gel of 15 mm diameter and 0.6 mm thickness sandwiched between the PTFE and PDMS layers. Last, a 9.5 mm hole was punched in the middle of an  $\sim$ 3.5 in.<sup>2</sup> piece of tan-colored medical tape (3M, #9907). This tape was then placed on top of the sensor housing layer (Figure 1F) to seal all layers within the sensor and to create a visible window of the thin H<sub>2</sub> sensing gel on top of the whitecolored PTFE layer. The final sensor was removed from the glass slide by using a razor blade to section an  $\sim 3$  in.<sup>2</sup> square of the layered assembly. A cross-sectional schematic with dimensions of the final sensor with the final liner of the medical tape removed is shown in Figure 1G. The overall thickness of the H2 sensing gel was 0.6 mm and was determined as the sum of the thicknesses of the 0.5 mm machined protrusion in Figure S1A (SI) and the 0.10 mm thickness of the gasket tape.

Gas Flow Setups: Determining the Flow Rate and Concentration of H<sub>2</sub> to Deliver to Visual H<sub>2</sub> Sensors. H<sub>2</sub> and N2 gas tanks were fitted with appropriate regulators and connected to the inlets of a gas proportioning rotameter (GPR) containing two separate flow tubes for H<sub>2</sub> and N<sub>2</sub> gases via stainless-steel tubing. Varying the scale readings of the GPR flow tubes for H<sub>2</sub> and N<sub>2</sub> gases permitted the creation of a sample mixture of H<sub>2</sub>/N<sub>2</sub> gas at a defined volume to volume ratio (V/V) and micromolar concentration. The calibrated flow rates of H2 and N2 gases from the GPR flow tubes at various scale readings were provided by the manufacturer and reported elsewhere. 32 The outlet of the GPR was connected to a single flow tube rotameter, which was then connected to a three-way valve. One outlet of the three-way valve allowed gas flow to vent, while the other was connected to PTFE tubing with a reducing union for gas flow to visual H2 sensors (Figure S2, SI).

The flow rate and concentration of H<sub>2</sub> delivered to visual H<sub>2</sub> sensors were determined by methods described previously. First, the apparatus in Figure S3 (SI) was used such that the PTFE tubing was connected to a DryCal DC-Lite flow calibrator via Tygon tubing to measure the flow rate of pure N<sub>2</sub> from the single rotameter flow tube at various scale readings through the PTFE tubing, of which the results are summarized in Table S1 (SI). It was deemed hazardous to measure H<sub>2</sub> flow using the DryCal DC-Lite flow calibrator and apparatus in Figure S3 (SI) due to potential sparking hazards. Thus, flow rates of sample gases containing H<sub>2</sub> coming from the single flow tube rotameter through the PTFE tubing at various scale readings were calculated theoretically using the data in Table S1 (SI), amperometrically measured concentrations of H<sub>2</sub> in the gas sample, and equations described elsewhere.<sup>32</sup> Nine gas samples containing H2 at various concentrations balanced in N<sub>2</sub> were prepared and used for visual H<sub>2</sub> sensor and control experiments. The H<sub>2</sub> concentration of each gas sample, in micromolar, was measured using a previously calibrated amperometric H<sub>2</sub> sensor (H<sub>2</sub>-NP-6076) as described previously.<sup>32</sup> These measurements permitted calculation of the volume percentages of  $H_2$  (% $V_{H_2}$ ) and  $N_2$  (% $V_{N_2}$ ) as well as the average molecular weights (MW $_{\mathrm{avg.}}$ ) and densities ( $ho_{\mathrm{mix}}$ ) of each sample gas, and these results are summarized in Table S2 (SI). Obtaining  $\rho_{mix}$  values permitted theoretical calculation of the flow rates of each sample gas at various scale readings (Table S3, SI). Plots of flow rate versus scale reading were made for each sample gas and fit to quadratic functions (Figure S4, SI), which could then be solved for the necessary scale reading of the single flow tube rotameter to deliver the sample gas at a desired flow rate.<sup>32</sup> Unless otherwise stated, a flow rate of 24.0 mL/min was used for all experiments described herein.

**Determining the Visual H**<sub>2</sub> **Sensor Response Using ImageJ.** The apparatus in Figure S5 (SI) was used to deliver  $H_2$  to visual  $H_2$  sensors while videos were simultaneously recorded with a smartphone. A piece of Tygon tubing (1/4 in. i.d., 3/8 in. o.d.) was cut and inserted into the 3/8 in. throughhole of the donor compartment from a Franz diffusion cell. Using an O-ring, the PTFE tubing (3/16 in. i.d., 1/4 in. o.d.) connected to the gas flow apparatus was fed through the Tygon tubing and donor compartment such that the end of the PTFE tubing was flushed against the surface of the donor compartment. Visual  $H_2$  sensors were affixed tightly on top of the donor compartment to allow flow of the sample gas into the visual  $H_2$  sensor by removing the liner of the medical tape.

A scale drawing of gas flow into the visual H2 sensor is provided in Figure S6 (SI). To monitor color changes that occurred during exposure to H2, a smartphone was mounted  $\sim$ 6" above the visual H<sub>2</sub> sensor and videos were recorded at 30 frames/s. VLC media player was used to convert videos from the smartphone to several pictures at 1 frame/s. ImageJ software was used to analyze pictures of the visual H<sub>2</sub> sensor area during gas exposure. Histograms of the red, green, blue, and brightness color channels of several images of the visual H<sub>2</sub> sensor surface before and during gas exposure were obtained using a macro function provided by ImageJ.<sup>34</sup> The mean values in the histograms of the red color channels were used to define the visual H<sub>2</sub> sensor response. Specifically, the quantity  $r_t/r_0$ was used where  $r_0$  and  $r_t$  denote the red color channel mean of the visual H<sub>2</sub> sensor area before and after gas exposure, respectively.

Reproducibility in the Visual H<sub>2</sub> Sensor Response, the Effects of Flow Rate, and Testing Permeability of H<sub>2</sub> through the Sensor Housing Layer. The reproducibility in the visual H<sub>2</sub> sensor response was studied by exposing five sensors to 800  $\mu$ M H<sub>2</sub> and five sensors to 103  $\mu$ M H<sub>2</sub> while the quantity  $r_t/r_0$  was measured. The effects of flow rate on the visual H<sub>2</sub> sensor response were investigated by flowing 47.6  $\mu$ M H<sub>2</sub> at rates of 5.28, 8.19, 40.5, and 62.5 mL/min while  $r_t/r_0$ was measured. To test whether H2 permeated through the sensor housing layer of the visual  $H_2$  sensor during gas flow, a previously calibrated amperometric H<sub>2</sub> sensor (H<sub>2</sub>-NPLR-011633) was mounted above a visual H<sub>2</sub> sensor placed within the apparatus in Figure S7 (SI) such that the tip of the amperometric H2 sensor made firm contact with the sensor housing layer above the  $H_2$  sensing gel.  $H_2$  (800  $\mu$ M) was flowed into the visual H<sub>2</sub> sensor while measurements of the H<sub>2</sub> concentration, via the amperometric sensor, and the quantity of  $r_t/r_0$ , via ImageJ, were made simultaneously.

Determining the Amounts of Au and Pd in the Au-Pd NP Master Solution via ICP-MS. The amounts Au and Pd in the Au-Pd NP master solution were calculated from ICP-MS measurements. All glassware were cleaned in 10% (m/V) HNO<sub>3</sub> and rinsed with DI water before use. Standard stock solutions of Pd and Au for calibrations were prepared at 1000 ppm using a Pd ICP-MS standard and HAuCl<sub>4</sub>·3H<sub>2</sub>O. Standards with concentrations of 0, 0.5, 1, 2, 5, 8, 10, and 15 ppb were prepared from the stock solutions. The solvent for Pd standards and Pd sample analyses was 2% HNO<sub>3</sub>, while the solvents for Au standards and Au sample analyses were 2% HNO<sub>3</sub> and 1% HCl, respectively. Calibration curves for Pd and Au were established as shown in Figures S8 and S9 (SI). A total of six samples of Au-Pd NP master solution were prepared for ICP-MS analysis where three were used to determine the Pd content, while three were used to determine the Au content. To prepare such samples, the Au-Pd NP master solution was first sonicated for 10 min prior to use. Ten microliters of the Au-Pd NP master solution was diluted with 40  $\mu$ L of DI water and then digested overnight with 450  $\mu$ L of aqua regia (1 part HNO<sub>3</sub> and 3 parts HCl). The mixture was further diluted the next day, and ICP-MS analyses were performed. The dilution factors of the samples for Au analysis were ×31,500 and ×6300 for Pd. The concentrations of all Au-Pd NP samples were within the calibration range for each metal. The raw data are shown in Tables S4 and S5 (SI).

**Control Experiments.** Using the apparatus in Figure S5 (SI), a series of control experiments were performed by flowing pure  $H_2$  or  $N_2$  into samples that were prepared

according to Figure 1 but had different combinations of materials in the AA hydrogel matrix (Table S6, SI) to determine these effects on the  $r_t/r_0$  signal. To ensure that the  $r_t/r_0$  signal remained stable during the data collection interval, a visual H<sub>2</sub> sensor containing resazurin and Au-Pd NPs in the AA hydrogel matrix was monitored without any gas flow (experiment 1, Table S6, SI). A series of controls using N<sub>2</sub> (experiments 2-6, Table S6, SI) and H<sub>2</sub> (experiments 7-11, Table S6, SI) were then conducted. The agarose and alginate compositions in the AA hydrogels for all control experiments were 4.425 mL of agarose solution combined with 5.000 mL of alginate solution. Samples containing resazurin had 5.25  $\times$ 10<sup>-5</sup> mmol/mL of total hydrogel solution. Samples containing NPs had 0.5% (V/V) concentrations in the total volume of hydrogel solution. Solutions were injected into sensors using syringes. The nanoparticle solutions used in these experiments were synthesized as described previously.<sup>32</sup>

# ■ RESULTS AND DISCUSSION

Photographs of Visual  $H_2$  Sensors Exposed to Various Concentrations of  $H_2$ . Photographs of seven different sensors each exposed to a different concentration of  $H_2$  at 24.0 mL/min are shown in Figure 2. It is evident that visual

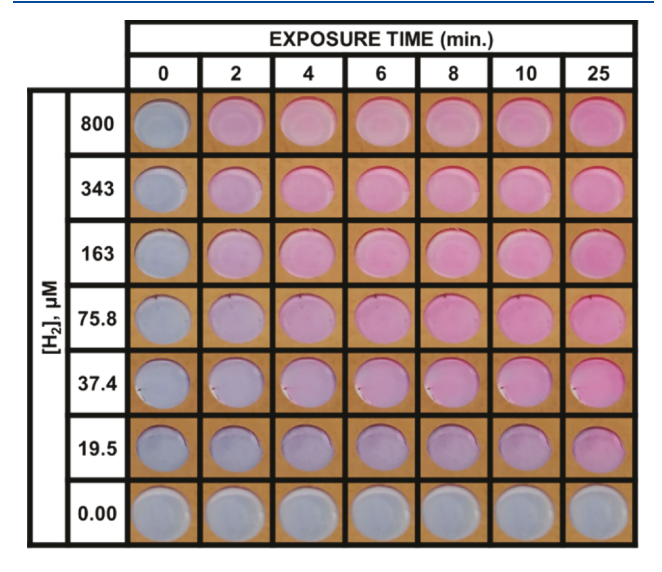


**Figure 2.** Photographs of seven visual  $H_2$  sensors exposed to  $H_2$  at a flow rate of 24.0 mL/min and concentrations of 0.00, 19.5, 37.4, 75.8, 163, 343, and 800  $\mu$ M at 0, 2, 4, 6, 8, 10, and 25 min of exposure.

blue to pink color changes occurred within sensors exposed to  $H_2$  at concentrations  $\geq 37.4~\mu\text{M}$ , while the sensor exposed to 19.5  $\mu$ M  $H_2$  changed color from blue to purple/pink. These data show that the resazurin molecules within sensors exposed to  $H_2$  at  $\geq 37.4~\mu\text{M}$  were fully converted to resorufin after  $\sim 25$  min. However, the sensor exposed to 19.5  $\mu$ M  $H_2$  underwent partial conversion in which some, but not all, of the resazurin molecules were converted to resorufin by  $H_2$ . No significant color change could be detected for the sensor exposed to 0.00  $\mu$ M  $H_2$ , i.e., 100%  $N_2$ .

Defining the Visual  $H_2$  Sensor Response Using ImageJ. Using the visual  $H_2$  sensor exposed to 75.8  $\mu$ M  $H_2$  as an example, Figure S10 (SI) shows how the mean values of the red, green, blue, and brightness color channels measured via ImageJ changed over time during  $H_2$  exposure. The mean value of the red color channel underwent the largest change,

and thus, the  $r_t/r_0$  quantity provided the best metric to define and measure the visual H<sub>2</sub> sensor response. Figure 3 displays

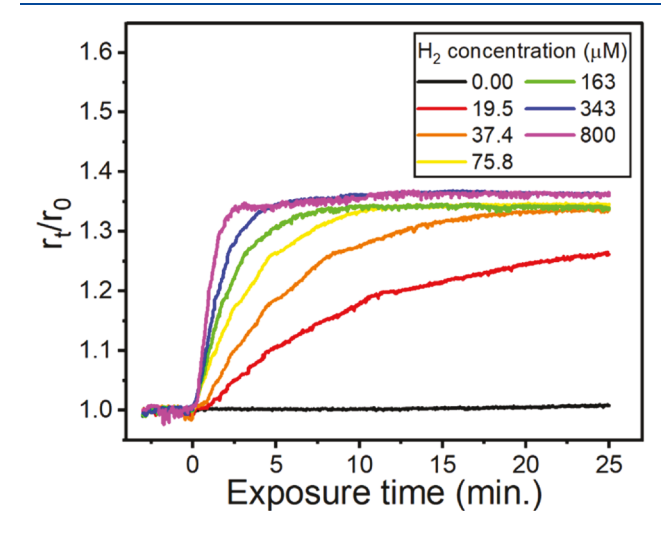


**Figure 3.** Plots of  $r_{\rm t}/r_0$  versus exposure time to H<sub>2</sub> at 0.00, 19.5, 37.4, 75.8, 163, 343, and 800  $\mu$ M concentrations at a 24.0 mL/min flow rate showing the response of the visual H<sub>2</sub> sensor.

the  $r_{\rm t}/r_0$  quantity of sensors as a function of exposure time to H<sub>2</sub> at various concentrations. Exposure to the highest concentration of  $H_2$  shows a rapid increase in  $r_t/r_0$  that abruptly plateaus when all of the resazurin is consumed by reaction with H<sub>2</sub>. Lowering the H<sub>2</sub> concentrations gives a slower increase in  $r_t/r_0$ , but all curves plateaued at approximately the same value except the lowest concentration, which provides insufficient H2 to completely react with all the resazurin in 25 min. These data demonstrate how the visual H<sub>2</sub> sensor response with time is nonlinear and dependent upon the exposure time and H2 concentration. Importantly, the rate at which the visual H2 sensors change color, for example, during the first 2 min of H2 exposure, is H2 concentrationdependent since the slope of the plots in Figure 3 during the early exposure time dramatically increased with the increasing concentration of  $H_2$ .

Visual H<sub>2</sub> Sensor Response as a Function of H<sub>2</sub> **Concentration.** The visual H<sub>2</sub> sensor response as a function of the large H<sub>2</sub> concentration range can be defined in a variety of ways such as the  $r_t/r_0$  value at a particular exposure time or the slope of the  $r_t/r_0$  vs exposure time plot over the course of a particular exposure time. In order to capture the visual H<sub>2</sub> sensor response over a large H<sub>2</sub> concentration range, we observed both of the aforementioned cases during the first 2 min, deemed method 1 and method 2 (Figure 4). In both cases, the visual H<sub>2</sub> sensor response for the two methods over a large concentration range is nonlinear. For method 1, the raw  $r_{\rm t}/r_{\rm 0}$  values for each sensor after 2.00 min of H<sub>2</sub> exposure, defined as  $r_{t_{200 \text{ min}}}/r_0$ , were plotted versus H<sub>2</sub> concentration (Figure 4, black circular data points, left-ordinate y-axis). For method 2, the  $r_t/r_0$  versus exposure time plots in Figure 3 were examined for each sensor at 2.00 min of H<sub>2</sub> exposure (Figure S11, SI). The slopes, defined as  $\delta(r_{t_{2.00\,\mathrm{min}}}/r_0)/\delta t_{2.00\,\mathrm{min}}$  , yintercepts, and R2 values of each data set were calculated (Table S7, SI). The values of  $\delta(r_{\rm t_{2.00\,min}}/r_0)/\delta t_{\rm 2.00\,min}$  were then plotted versus H2 concentration (Figure 4, red square data points, right-ordinate y-axis).

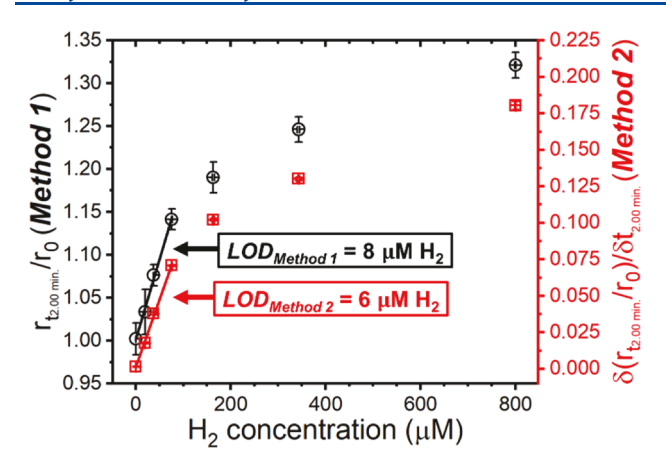


Figure 4. Defining the visual H2 sensor response via method 1 in which the raw  $r_t/r_0$  values for each visual H<sub>2</sub> sensor after 2.00 min of  $H_2$  exposure, defined as  $r_{\rm t_{2.00\,min}}/r_0$ , were plotted versus  $H_2$ concentration (black circular data points, left-ordinate y-axis). Defining the visual sensor response via method 2 in which the slopes of the  $r_t/r_0$  versus exposure time plot for 2.00 min of H<sub>2</sub> exposure, defined as  $\delta(r_{\rm t_{2.00\,min}}/r_0)/\delta t_{\rm 2.00\,min}$ , were plotted versus H<sub>2</sub> concentration (red square data points, right-ordinate y-axis). Estimation of the visual H<sub>2</sub> sensor LOD based on the sensor response via methods 1 and 2. Linear fitting to the black circular data points yielded an equation of y =  $(1.87 \times 10^{-3} \pm 8.8 \times 10^{-5})x + (1.00 \pm 3.8 \times 10^{-3}), R^2 = 1.0.$ Linear fitting to the red square data points yielded the equation  $y = (9.25 \times 10^{-4} \pm 3.4 \times 10^{-5})x + (1.30 \times 10^{-3} \pm 1.5 \times 10^{-3}), R^2 = 1.0.$ All linear fits were made using data points at  $\leq 75.8 \, \mu M \, H_2$ . The xerror bars stem from uncertainties in the electrochemically measured H<sub>2</sub> concentrations of gas samples and in all cases are smaller than the data points presented. The y-error bars stem from uncertainties in the values of  $r_{\rm t_{2.00\,min}}/r_0$  and  $\delta(r_{\rm t_{2.00\,min}}/r_0)/\delta t_{\rm 2.00\,min}$ . The *y*-error bars are smaller than the red square data points associated with method 2.

Estimating the Limit of Detection of the Visual H<sub>2</sub> Sensor. Though the visual H<sub>2</sub> sensor response defined by methods 1 and 2 over a large concentration range in Figure 4 were nonlinear, examination of the data at  $\leq$ 75.8  $\mu$ M H<sub>2</sub> permitted an estimation of the limit of detection (LOD) of the visual H2 sensor using a smartphone and ImageJ analyses for detection. This was accomplished by plotting the data at  $\leq$ 75.8  $\mu$ M H<sub>2</sub> from Figure 4, fitting linear equations to the data (shown as solid lines in Figure 4) to determine the slopes (s), y-intercepts, and standard errors in the linear regression (SE(y)) and then employing eq 3 to calculate the LOD.<sup>35</sup> The data and results from these analyses for methods 1 and 2 are tabulated in Tables S8 and S9 (SI). The LODs based on methods 1 and 2 were 8 and 6  $\mu$ M H<sub>2</sub>, respectively, and suggest that the visual H<sub>2</sub> sensor detection range is adequate for the intended application of noninvasively monitoring in vivo Mg-alloy implant biodegradation. Interestingly, the LODs via methods 1 and 2 were similar yet statistically different because the sensor response via method 1 had slope and SE(y)values that were 2 and 2.6 times larger than those of method 2, respectively. The smaller magnitude of SE(y) for the sensor response via method 2 resulted in a lower LOD.

$$LOD = \frac{3 \times SE(y)}{s}$$
 (3)

**Reproducibility in the Visual H<sub>2</sub> Sensor Response.** The reproducibility in the visual H<sub>2</sub> sensor response was evaluated by making five measurements, each with a different

sensor, at two different  $H_2$  concentrations, and the results are summarized in Table S10. These data exhibit reasonable reproducibility in the magnitudes of  $r_{\rm t_{2.00~min}}/r_0$  and  $\delta(r_{\rm t_{2.00~min}}/r_0)/\delta t_{\rm 2.00~min}$ . The variability in these results was attributed to small variations in sensor fabrications such as the overall thickness of the sensing layer and human error from injecting the sensing gel into the layered assembly by hand.

Effects of Flow Rate on the Visual  $H_2$  Sensor Response. The effects of flow rate of a single concentration of  $H_2$  on the visual  $H_2$  sensor response are shown in Figure S12. At the flow rates and  $H_2$  concentrations studied herein, the effects are negligible at flow rates of  $\geq$ 40.5 mL/min since the  $r_t/r_0$  versus exposure time responses are similar (blue and green traces in Figure S12). However, the color change response time of the visual  $H_2$  sensor increased significantly when flowing  $H_2$  at 8.19 and 5.28 mL/min (red and black traces in Figure S12, respectively). At slower flow rates, the permeation of  $H_2$  into the sensor is very slow and therefore increases the color change response time. This can be seen for the experiment at a 5.28 mL/min flow rate in which the  $r_t/r_0$  signal does not begin to increase until after  $\sim$ 2.6 min of  $H_2$  exposure.

Testing the Permeability of H<sub>2</sub> through the Sensor **Housing Layer.** The permeability of H<sub>2</sub> through the sensor housing layer during gas flow was examined to determine if a majority of the H2 flows directly through the visual H2 sensor or if the H<sub>2</sub> sensing gel uses H<sub>2</sub> efficiently to induce visual color changes. Figure S13 shows the visual H<sub>2</sub> sensor response (black trace, left-ordinate y-axis), while an amperometric  $H_2$ sensor was placed above and made firm contact with the sensor housing layer to measure the H<sub>2</sub> concentration potentially permeating above the visual H<sub>2</sub> sensor (red square data points, right-ordinate y-axis). These data demonstrate that a small amount of H<sub>2</sub> could be detected electrochemically, exiting the top covering of the visual H2 sensor during gas delivery since the electrochemical trace (Figure S13, red square data points, right-ordinate y-axis) increased during H<sub>2</sub> exposure. To calculate the concentration of H2 that permeated through the visual H<sub>2</sub> sensor ([H<sub>2</sub>]<sub>permeate</sub>), eq S1 (SI) was used where  $[H_2]_{\text{during flow}}$  and  $[H_2]_{\text{no flow}}$  are the average electrochemically measured H<sub>2</sub> concentrations during the last 5 min of gas flow and under no gas flow, respectively. From the data in Figure S13 (red square data points, right-ordinate y-axis), the  $[H_2]_{permeate}$  value was calculated to be 1.88  $\pm$  0.14  $\mu$ M. However, this data suggests that the sensor housing layer was sufficiently thick to prevent significant H<sub>2</sub> permeation through the top layer of the visual H<sub>2</sub> sensor and that the H<sub>2</sub> sensing gel uses H<sub>2</sub> efficiently to induce visual color changes.

Calculating the Amounts of Resazurin, Pd, and Au in the Visual  $H_2$  Sensor. The total amounts of resazurin, Pd, and Au in the visual  $H_2$  sensor were calculated to understand the relative amounts of each component within the  $H_2$  sensing gel. The total number of millimoles of resazurin in the visual  $H_2$  sensor ( $n_{\rm resaz}$ ) was estimated by first calculating the void volume ( $V_{\rm void}$ ) between the PTFE tape and sensor housing layer. The parameter  $V_{\rm void}$  is illustrated in Figure S14A (SI), which is a cross section of the visual  $H_2$  sensor constructed in Figure 1D prior to injection of the  $H_2$  sensing gel. A three-dimensional representation of  $V_{\rm void}$  with dimensions is shown in Figure S14B (SI) and comprises three cylinders with volumes denoted as  $V_1$ ,  $V_2$ , and  $V_3$ . The parameter  $V_{\rm void}$  was then calculated according to eqs S2–S5 (SI) and had a value of

115  $\mu$ L. The value of  $n_{\rm resaz}$  was calculated via eq S6 (SI) where  $C_{\rm resaz_{\rm gel}}$  is the concentration of resazurin in the total volume of the H<sub>2</sub> sensing gel solution (i.e.,  $5.25 \times 10^{-5}$  mmol/mL of total hydrogel solution). The value of  $n_{\rm resaz}$  was calculated to be 6.0  $\times$  10<sup>-6</sup> mmol (eq S7, SI).

The ppm concentrations of Pd  $(C_{Pd})$  and Au  $(C_{Au})$  in the Au-Pd NP master solution were calculated from ICP-MS data using eq S8 (SI) where  $\tilde{y}$ , b, m, and DF are the average counts per second (cps) signal from three replicate measurements, the y-intercept of the calibration curve, the slope of calibration curve, and the dilution factor, respectively. The values  $C_{Pd}$  and  $C_{\rm Au}$  were 79  $\pm$  8.0 ppm and 455  $\pm$  5.3 ppm, respectively (eqs S9 and S10, SI). To estimate the millimole amounts of Pd and Au in the visual H<sub>2</sub> sensor ( $n_{Pd}$  and  $n_{Au}$ ), eq S11 (SI) was first employed to calculate the total volume of Au-Pd NPs in the visual  $H_2$  sensor  $(V_{Au-Pd\ NPs})$  knowing  $V_{void}$  and the volume of Au-Pd NPs per total volume of  $H_2$  sensing gel solution ( $V_{\rm Au-Pd~NPs/gel}$ ), where 50  $\mu \rm L$  of Au-Pd NPs was used per 10.0 mL total volume of hydrogel solution). The quantity  $V_{\rm Au-Pd\ NPs}$  was calculated to be 5.75  $\times$  10<sup>-1</sup>  $\mu \rm L$  (eq S12, SI). Values of  $n_{\rm Pd}$  and  $n_{\rm Au}$  were then calculated to be  $4.3 \times 10^{-7}$ and  $1.3 \times 10^{-6}$  mmol, respectively, using the molar masses of Pd (MW<sub>Pd</sub>) and Au (MW<sub>Au</sub>) (eqs S13-S16, SI). Based on these results for the H<sub>2</sub> sensing gels used herein, for every 1 mmol of Pd in the visual H2 sensor, 14 mmol of resazurin and 3.0 mmol of Au are present. Understanding the relative amounts of these components will aid future sensor optimization.

**Control Experiments.** Control experiments were performed to clearly establish that the visual  $H_2$  sensor response was due entirely to the reaction with  $H_2$ . From experiment 1 in Table S6 (SI), it was observed that the  $r_t/r_0$  signal was very stable and remained nearly constant during measurement with no gas flow (Figure S15, SI). Similar results were observed in experiments 2–11 (Table S6, SI) as  $N_2$  and  $H_2$  were flowed into samples. In each case, negligible changes in the  $r_t/r_0$  value were measured (Figures S16 and S17, SI). These observations confirm that  $N_2$  had no effect on the observed color changes within visual  $H_2$  sensors and that color changes only arose when  $H_2$  reacted with resazurin in the presence of Au-Pd NP catalysts loaded within the AA hydrogel matrix.

#### CONCLUSIONS

We have successfully developed a novel visual H<sub>2</sub> sensor prototype composed of resazurin and Au-Pd NPs incorporated into a thin AA hydrogel matrix that rapidly changed color from blue to pink upon exposure to various levels of H<sub>2</sub> at a known flow rate. The blue to pink color changes within visual H2 sensors proceeded via the irreversible reaction pathway described in eq 2 in which resazurin was converted by H<sub>2</sub> in the presence of Au-Pd NPs to resorufin. The color changes of visual H<sub>2</sub> sensors exhibited reasonable reproducibility from sensor to sensor and could be easily detected using a smartphone to monitor the sensor surface during H<sub>2</sub> exposure, and then employing freeware for data processing. Defining the visual H2 sensors response via methods 1 and 2 under the conditions described herein revealed LODs of 8 and 6  $\mu$ M, respectively. Thus, the visual H2 sensor developed in this work is potentially useful for our intended application of noninvasively monitoring the in vivo corrosion of Mg implants in medical research and clinical settings.

The effects of flow rate on the visual  $H_2$  sensor response were negligible at flow rates of  $\geq$ 40.5 mL/min, while the color change response time increased significantly when flowing  $H_2$  at 8.19 and 5.28 mL/min. Testing the permeability of  $H_2$  through the sensing housing layer of the visual  $H_2$  sensor revealed that only a small concentration of  $H_2$  could be detected on the top layer of the visual  $H_2$  sensor, suggesting that the sensor housing layer was sufficiently thick to prevent significant  $H_2$  permeation through the top layer of the visual  $H_2$  sensor and that the  $H_2$  sensing gel uses  $H_2$  efficiently to induce visual color changes.

Though the visual  $H_2$  sensor in this work was developed for the target application of monitoring the biodegradation of Mgalloy implants *in vivo*, the sensor developed herein is potentially useful for other  $H_2$  sensing applications. Future works will involve optimizing the sensor response, improving the sensitivity, animal studies, and product development.

# ASSOCIATED CONTENT

# Supporting Information

The Supporting Information is available free of charge at https://pubs.acs.org/doi/10.1021/acs.analchem.1c01276.

Description of the chemicals, materials, and instrumentation used throughout the study; figures and tables describing sensor housing layer fabrication; various gas flow setups and determinations of flow rates of  $N_2$ ,  $H_2$ , and H<sub>2</sub>/N<sub>2</sub> gases; scale drawing of gas flow into visual H<sub>2</sub> sensors; ICP-MS analyses; changes in various color channels within sensors measured by ImageJ during exposure to  $H_2$ , plots of  $r_t/r_0$  versus exposure time for determining the visual H2 sensor response as a function of H<sub>2</sub> concentration via method 2; data for calculating sensor LODs via methods 1 and 2; reproducibility of the visual H<sub>2</sub> sensor response; effects of flow rate; testing the permeability of H<sub>2</sub> through the sensor housing layer; schematics and equations for calculating the amounts of resazurin, Pd, and Au in the visual H2 sensor as well as  $[H_2]_{permeate}$ ; and data for control experiments (PDF)

## AUTHOR INFORMATION

### **Corresponding Authors**

Peng Zhang — Department of Chemistry, University of Cincinnati, Cincinnati, Ohio 45221-0172, United States; orcid.org/0000-0003-3902-6876; Phone: 513-556-9222; Email: zhangph@ucmail.uc.edu

William R. Heineman — Department of Chemistry, University of Cincinnati, Cincinnati, Ohio 45221-0172, United States; orcid.org/0000-0003-2428-5445; Phone: 513-556-9210; Email: heinemwr@ucmail.uc.edu

#### **Authors**

Michael E. Smith — Department of Chemistry, University of Cincinnati, Cincinnati, Ohio 45221-0172, United States

Daniel P. Rose — Department of Chemistry, University of Cincinnati, Cincinnati, Ohio 45221-0172, United States

Xiaoyu Cui — Department of Chemistry, University of Cincinnati, Cincinnati, Ohio 45221-0172, United States

Angela L. Stastny — Department of Chemistry, University of Cincinnati, Cincinnati, Ohio 45221-0172, United States

Complete contact information is available at: https://pubs.acs.org/10.1021/acs.analchem.1c01276

### **Author Contributions**

M.E.S, W.R.H., and P.Z. designed the research project. M.E.S. wrote the manuscript and carried out all experiments and measurements except where noted. D.P.R. assisted with conceptualizing the visual H<sub>2</sub> sensor design and provided ideas for making the H<sub>2</sub> sensing gel. X.C. carried out all experiments involving ICP-MS. A.L.S. critically revised the manuscript and aided with gas flow setups and ImageJ software.

#### Notes

The authors declare no competing financial interest.

# ACKNOWLEDGMENTS

The authors gratefully acknowledge the National Science Foundation for financial support (IIP-2016475). Jon Klett is acknowledged for his assistance with tape samples. Michael G. Elliott is acknowledged for assistance with the DryCal DC-Lite flow calibrator.

# **■** REFERENCES

- (1) Kuhlmann, J.; Bartsch, I.; Willbold, E.; Schuchardt, S.; Holz, O.; Hort, N.; Höche, D.; Heineman, W. R.; Witte, F. *Acta Biomater.* **2013**, 9, 8714–8721.
- (2) Zhao, D.; Wang, T.; Hoagland, W.; Benson, D.; Dong, Z.; Chen, S.; Chou, D. T.; Hong, D.; Wu, J.; Kumta, P. N.; Heineman, W. R. Acta Biomater. **2016**, 45, 399–409.
- (3) Staiger, M. P.; Pietak, A. M.; Huadmai, J.; Dias, G. Biomaterials **2006**, 27, 1728–1734.
- (4) Witte, F.; Calliess, T.; Windhagen, H. Orthopade 2008, 37, 125-130
- (5) Han, H. S.; Loffredo, S.; Jun, I.; Edwards, J.; Kim, Y. C.; Seok, H. K.; Witte, F.; Mantovani, D.; Glyn-Jones, S. *Mater. Today* **2019**, 23, 57–71
- (6) Zhao, D.; Wu, J.; Chou, D.-T.; Hoagland, W.; Benson, D.; Dong,Z.; Kumta, P. N.; Heineman, W. R. JOM 2020, 72, 1851–1858.
- (7) Agrawal, C. M. JOM 1998, 50, 31-35.
- (8) Zhao, D.; Wang, T.; Kuhlmann, J.; Dong, Z.; Chen, S.; Joshi, M.; Salunke, P.; Shanov, V. N.; Hong, D.; Kumta, P. N.; Heineman, W. R. Acta Biomater. 2016, 36, 361–368.
- (9) Uhthoff, H. K.; Poitras, P.; Backman, D. S. J. Orthop. Sci. 2006, 11, 118-126.
- (10) Witte, F. Acta Biomater. 2010, 6, 1680-1692.
- (11) Haynes, D. R.; Boyle, S. J.; Rogers, S. D.; Howie, D. W.; Vernon-Roberts, B. Clin. Orthop. Relat. Res. 1998, 223–230.
- (12) Lhotka, C.; Szekeres, T.; Steffan, I.; Zhuber, K.; Zweymüller, K. J. Orthop. Res. 2003, 21, 189–195.
- (13) Wang, J. Y.; Wicklund, B. H.; Gustilo, R. B.; Tsukayama, D. T. *Biomaterials* **1996**, *17*, 2233–2240.
- (14) Niki, Y.; Matsumoto, H.; Suda, Y.; Otani, T.; Fujikawa, K.; Toyama, Y.; Hisamori, N.; Nozue, A. *Biomaterials* **2003**, *24*, 1447–1457.
- (15) Zhao, D.; Brown, A.; Wang, T.; Yoshizawa, S.; Sfeir, C.; Heineman, W. R. Acta Biomater. 2018, 73, 559–566.
- (16) Hermawan, H. Prog. Biomater. 2018, 7, 93-110.
- (17) Chaya, A.; Yoshizawa, S.; Verdelis, K.; Noorani, S.; Costello, B. J.; Sfeir, C. J. Oral Maxillofac. Surg. 2015, 73, 295–305.
- (18) Chaya, A.; Yoshizawa, S.; Verdelis, K.; Myers, N.; Costello, B. J.; Chou, D.-T.; Pal, S.; Maiti, S.; Kumta, P. N.; Sfeir, C. *Acta Biomater.* **2015**, *18*, 262–269.
- (19) Yang, Y.; He, C.; Dianyu, E.; Yang, W.; Qi, F.; Xie, D.; Shen, L.; Peng, S.; Shuai, C. *Mater. Des.* **2020**, *185*, 108259.
- (20) Zhang, Y.; Xu, J.; Ruan, Y. C.; Yu, M. K.; O'Laughlin, M.; Wise, H.; Chen, D.; Tian, L.; Shi, D.; Wang, J.; Chen, S.; Feng, J. Q.; Chow, D. H. K.; Xie, X.; Zheng, L.; Huang, L.; Huang, S.; Leung, K.; Lu, N.; Zhao, L.; Li, H.; Zhao, D.; Guo, X.; Chan, K.; Witte, F.; Chan, H. C.; Zheng, Y.; Qin, L. Nat. Med. 2016, 22, 1160–1169.

- (21) Zhao, D.; Huang, S.; Lu, F.; Wang, B.; Yang, L.; Qin, L.; Yang, K.; Li, Y.; Li, W.; Wang, W.; Tian, S.; Zhang, X.; Gao, W.; Wang, Z.; Zhang, Y.; Xie, X.; Wang, J.; Li, J. Biomaterials 2016, 81, 84–92.
- (22) Cheng, P.; Han, P.; Zhao, C.; Zhang, S.; Wu, H.; Ni, J.; Hou, P.; Zhang, Y.; Liu, J.; Xu, H.; Liu, S.; Zhang, X.; Zheng, Y.; Chai, Y. *Biomaterials* **2016**, *81*, 14–26.
- (23) Schaller, B.; Saulacic, N.; Imwinkelried, T.; Beck, S.; Liu, E. W. Y.; Gralla, J.; Nakahara, K.; Hofstetter, W.; Iizuka, T. *J. Craniomaxillofac. Surg.* **2016**, *44*, 309–317.
- (24) Banerjee, P. Č.; Al-Saadi, S.; Choudhary, L.; Harandi, S. E.; Singh, R. *Mater.* **2019**, *12*, 1–21.
- (25) Choudhary, L.; Singh Raman, R. K. Acta Biomater. 2012, 8, 916-923.
- (26) Wang, J. L.; Xu, J. K.; Hopkins, C.; Chow, D. H. K.; Qin, L. Adv. Sci. 2020, 7, 1902443.
- (27) Paramitha, D.; Ulum, M. F.; Purnama, A.; Wickasono, D. H. B.; Noviana, D.; Hermawan, H. Monitoring Degradation Products and Metal Ions in Vivo. In *Monitoring and evaluation of biomaterials and their performance in vivo*; Narayan, R. J., Ed.; Woodhead Publishing: Cambridge, MA, 2017; pp. 19–44.
- (28) Liu, Y.; Herman, B. A.; Soneson, J. E.; Harris, G. R. *Ultrasound Med. Biol.* **2014**, *40*, 1001–1014.
- (29) Fazel, R.; Krumholz, H. M.; Wang, Y.; Ross, J. S.; Chen, J.; Ting, H. H.; Shah, N. D.; Nasir, K.; Einstein, A. J.; Nallamothu, B. K. N. Engl. J. Med. **2009**, 361, 849–857.
- (30) Zhao, D.; Wang, T.; Heineman, W. TrAC Trends Anal. Chem. **2016**, 79, 269-275.
- (31) Zhao, D.; Wang, T.; Nahan, K.; Guo, X.; Zhang, Z.; Dong, Z.; Chen, S.; Chou, D. T.; Hong, D.; Kumta, P. N.; Heineman, W. R. *Acta Biomater.* **2017**, *50*, 556–565.
- (32) Smith, M. E.; Stastny, A. L.; Lynch, J. A.; Yu, Z.; Zhang, P.; Heineman, W. R. *Anal. Chem.* **2020**, *92*, 10651–10658.
- (33) Zeng, Q.; Han, Y.; Li, H.; Chang, J. J. Mater. Chem. B 2015, 3, 8856–8864.
- (34) imageJ macro function. https://imagej.nih.gov/ij/macros/MeasureRGB.txt (accessed Jan 14, 2020).
- (35) Long, G. L.; Winefordner, J. D. Anal. Chem. 1983, 55, 713A-724A.